1   **Integration of 3D-Printed Micromixers and Spray Drying for Pulmonary Delivery of**

2   **Antimicrobial Microparticles**

3   Brayan J. Anaya[1], Aytug Kara[1], Rafaela Raposo[2], Diego F. Tirado[3], Aikaterini Lalatsa[4],

4   Elena González-Burgos[5*], D.R. Serrano [1,6*]

5

6   [1] Pharmaceutics and Food Technology Department, Faculty of Pharmacy, Universidad

7   Complutense de Madrid, Plaza Ramón y Cajal s/n, 28040 Madrid, Spain.

8   [2] Sección Departamental de Fisiología, Faculty of Pharmacy, Universidad Complutense de

9   Madrid (UCM), 28040 Madrid, Spain.

10   [3] Dirección Académica, Universidad Nacional de Colombia, Sede de La Paz, La Paz 202017,

11   Colombia.

12   [4] CRUK Formulation Unit, School of Pharmacy and Biomedical Sciences, University of

13   Strathclyde, John Arbuthnot Building, Robertson Wing, 161 Cathedral St, Glasgow G4 0RE,

14   UK

15   [5] Department of Pharmacology, Pharmacognosy and Botany, Faculty of Pharmacy,

16   Universidad Complutense de Madrid (UCM), 28040 Madrid, Spain.

17   [6] Instituto Universitario de Farmacia Industrial, Faculty of Pharmacy, Universidad
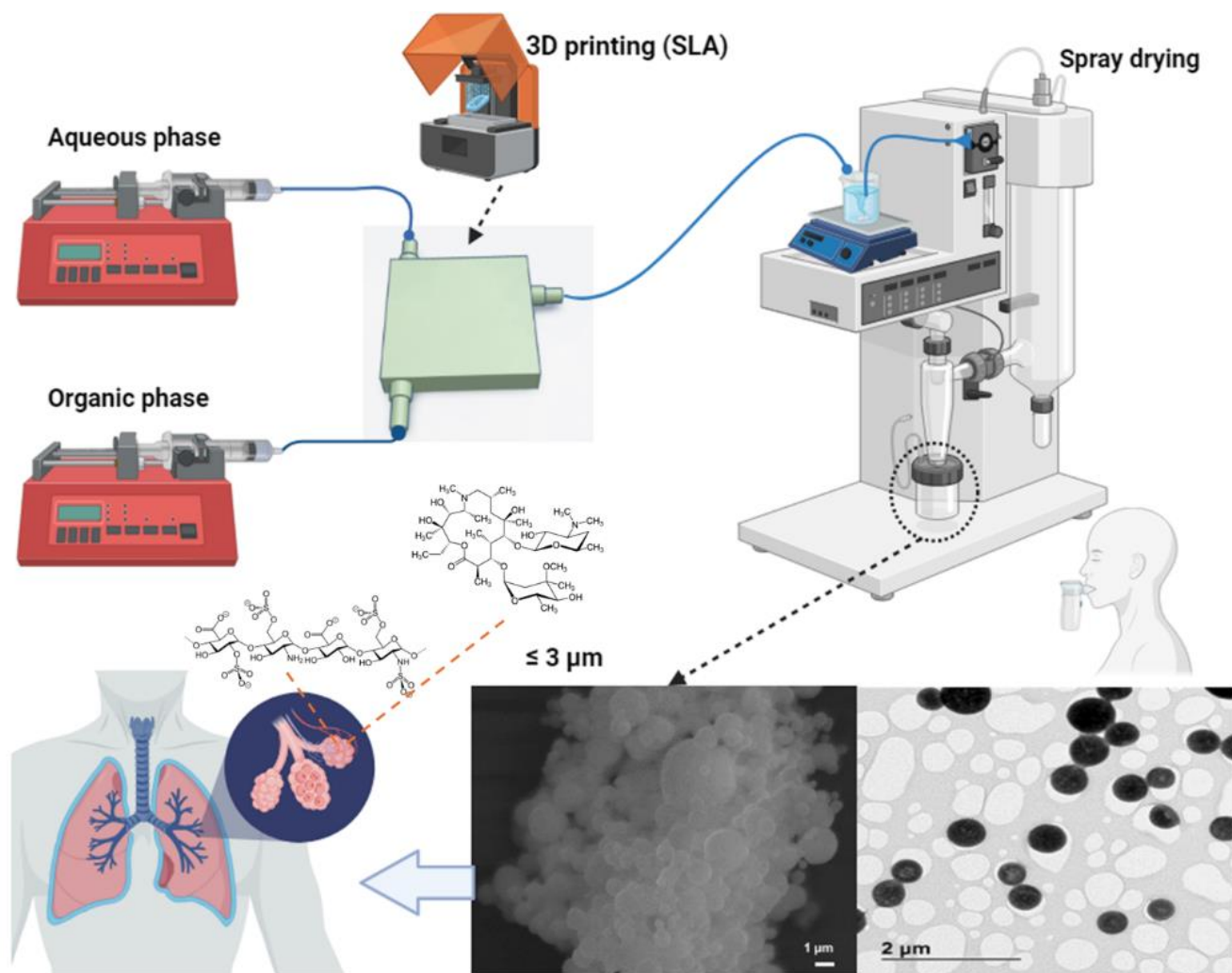
18   Complutense de Madrid, 28040, Madrid, Spain.

19

20   * Corresponding authors:

21   Dolores R Serrano – drserran@ucm.es

22   Elena Gonzalez Burgos – elenagon@ucm.es

23

24   **Graphical abstract**

26

27 **Abstract**

28 Pulmonary drug delivery is crucial for treating respiratory diseases, requiring precise particle

29 engineering for optimal therapeutic efficacy. This study demonstrates a novel integration of

30 3D-printed microfluidic micromixers with spray drying technology to produce inhalable

31 azithromycin (AZM) microparticles targeting lung delivery. The formulation demonstrated

32 effective deep lung deposition at both 30 L/min and 60 L/min flow rates. At 30 L/min, AZM-

33 loaded microparticles achieved enhanced performance with 1.2-fold higher Fine Particle

34 Fraction (FPF) < 5 µm and 1.4-fold higher FPF < 3 µm compared to 60 L/min. Microparticles

35 (25 mg) can deliver an efficacious dose of AZM to the lung, exceeding the reported

36 epidemiological cut-off for *Haemophilus influenzae* (4 mg/L) by approximately five-fold

37 while maintaining high human bronchial epithelial cell viability (> 94 %). The antibacterial

38 efficacy against *H. influenzae* was confirmed, demonstrating the therapeutic potential against

39 lung pathogens. The successful deep lung deposition at both air flow rates reflects the

40 robustness of the formulation design, making it suitable for diverse patient populations with

41 varying inspiratory capabilities, including children and elderly patients.

42 **Keywords:**

45

1. Introduction

Pulmonary drug delivery has emerged as a valuable approach for treating lung diseases such as asthma, chronic obstructive pulmonary disease (COPD), pulmonary arterial hypertension (PAH), and select pulmonary infections. While systemic antimicrobials administered orally or intravenously remain the standard treatment for pulmonary infections, localized drug delivery to the lungs offers the advantage of directly targeting the site of action, potentially enhancing therapeutic efficacy and minimizing systemic side effects. Devices such as dry powder inhalers (DPIs), metered dose inhalers (MDIs), and nebulizers facilitate efficient drug distribution and absorption by delivering particles with aerodynamic diameters ranging from 1 µm to 5 µm, optimizing deposition in the respiratory tract. Devices such as DPIs and nebulizers are preferred for antimicrobial delivery due to their ability to deposit higher doses into the lungs, while MDIs are primarily used for bronchodilator and corticosteroid administration [1-6].

In particular, DPIs offer several advantages, including deep lung deposition with high-dose delivery, ease of use, and minimized side effects. As breath-actuated devices, DPIs eliminate the need for coordinating inhalation with device activation, improving patient compliance. While their lower carbon footprint and cost-effectiveness are important environmental and economic benefits, compliance is primarily driven by their user-friendly design and consistent therapeutic outcomes compared to MDIs and nebulizers [7-9]. Traditionally, DPIs require inspiratory flow rates of 60 L/min for optimal drug particle deposition in the lungs, which can be challenging for patients with reduced respiratory capacity, such as those with severe COPD or asthma. By optimizing the aerodynamic particle size, DPIs can be designed to achieve effective deep lung deposition at lower flow rates (30 L/min or even lower), similar to MDIs and nebulizers [10-12].

The significant impact of COVID-19 on respiratory function, particularly in patients with pre-existing conditions such as bacterial infections, underscores the urgent need for innovative therapeutic strategies to address the unique challenges faced by these individuals [13-15]. The optimization of DPIs to achieve effective deep lung deposition at lower inspiratory flow rates offers a promising approach for patients with reduced respiratory capacity due to COVID-19 or other underlying conditions. By designing DPIs with optimized

76   aerodynamic particle sizes, these devices can deliver high doses to the lungs while
77   minimizing side effects. Developing DPIs specifically tailored to the needs of COVID-19
78   survivors and those with compromised lung function could significantly enhance therapeutic
79   outcomes and quality of life, highlighting the importance of ongoing research and innovation
80   in this field.

81   3D printing technologies have emerged as a transformative tool in pharmaceutical
82   applications, providing innovative solutions for treating lung diseases. This cutting-edge
83   technology enables the development of highly customized and patient-specific medical
84   devices, drug delivery systems, and complex tissue models, essential for addressing the
85   unique challenges associated with pulmonary conditions [16-21]. The capability of 3D
86   printing to produce intricate geometries and complex compositions with high precision
87   makes it particularly well-suited for creating devices used in lung drug delivery.

88   3D-printed microfluidic micromixers offer a compact and versatile platform for the synthesis
89   of particles ranging from nanometers to micrometers in size. These micromixers integrate
90   multiple unit operations, including processing, separation, reaction, and detection, enabling
91   rapid and efficient analysis of the synthesized particles. The incorporation of microreactors
92   and micromixers is essential for producing particles with uniform size distribution and
93   enhanced encapsulation efficiency. Precise control over particle size and distribution is
94   achieved by manipulating flow rates, solvents, surfactants, and polymer compositions within
95   simple and adaptable designs. This level of control is crucial for applications such as drug
96   delivery systems, where particle characteristics significantly influence the efficacy and
97   biodistribution of the encapsulated therapeutic agent [22-26].

98   The AZM-heparin inhalable co-formulation presents a novel approach to treating complex
99   respiratory infections, including COVID-19. AZM exhibits potent anti-inflammatory effects
100   in chronic respiratory diseases, significantly reducing exacerbations in COPD and cystic
101   fibrosis [27, 28]. AZM modulates the lung microbiota, enhancing anti-inflammatory
102   metabolites and mitigating pro-inflammatory responses in *Pseudomonas aeruginosa*
103   infections [29]. Crucially, AZM inhibits inflammasome activation, a key pathway in innate
104   immune responses, by reducing the secretion of IL-1 and other pro-inflammatory cytokines
105   [30]. This mechanism is particularly beneficial in respiratory diseases where excessive

106   inflammasome activation contributes to pathology. This multi-faceted action, targeting host
107   immunity, pathogen virulence, and inflammatory cascades, positions AZM as a key
108   therapeutic agent for complex respiratory conditions characterized by chronic inflammation
109   and recurrent infections [31-33]. Conversely, heparin exhibits dual efficacy in COVID-19
110   treatment. Its well-established anticoagulant properties reduce thromboembolic risks
111   associated with virus-induced endothelial damage, while its potential antiviral effects may
112   inhibit SARS-CoV-2 cellular entry and replication [34-37]. This multifaceted action
113   positions heparin as a critical therapeutic agent in managing the complex pathophysiology of
114   COVID-19, particularly for high-risk, critically ill patients. We have previously
115   demonstrated the synergistic combined effect between heparin and AZM against lung
116   pathogens [38].

117   The hypothesis underlying this work is that 3D-printed microfluidic micromixers could be
118   useful to tailor the particle size of DPI formulations enabling a continuous manufacture
119   methodology to enhance both yield and efficiency of the process. Microfluidic devices allow
120   for an effective mixing of drugs and excipients within their microchannels. The selection of
121   suitable solvents will guarantee controlled precipitation targeting the ideal particle size for
122   lung delivery. The integration of microfluidic micromixers with spray drying could tune the
123   final particle characteristics for an excellent particle lung deposition [25, 39-41]. Spray
124   drying is a scalable technology widely used by pharmaceutical industries for the manufacture
125   of dry powders [42-45]. We have previously demonstrated the feasibility of preparing AZM-
126   loaded microparticles using spray drying [38]. In this work, we will go beyond the state-of-
127   the-art to demonstrate the integration of a continuous manufacturing platform consisting of
128   a microfluidic micromixer coupled with spray drying. This combination of both technologies
129   is capable of controlling particle precipitation with an optimalparticle size towards
130   antibacterial inhalable microparticles targeting deep lung regions being less dependent on the
131   patient's inspiratory flow rate, thereby reducing interpatient variability and making the
132   devices suitable for a broader range of patients, including young children and the elderly. The
133   mixing process of AMZ-loaded microparticles was modelled using computational fluid
134   dynamics. Microparticles were fully characterised and *in vitro* lung deposition was assessed.
135   The biological activity was tested against mammalian cells and bacteria.

2. Material and methods

2.1. Materials

Heparin sodium salt (purity > 95 %), CAS # 9041-08-1 from porcine intestinal mucosa, Lot No. A0411030 (203.5 IU/mg, Acros organics) was purchased from Fisher Scientific (Madrid, Spain). Azithromycin (AZM) with purity ≥ 95 % was bought from Kemprotec (Cumbria, UK) while leucine with purity ≥ 98 % was purchased from Sigma Aldrich (Madrid, Spain). UV polymerizable commercial clear resin (405 nm) was obtained from Anycubic® (Shenzhen, China). Methanol (HPLC grade, purity: ≥ 99.9 %) was purchased from Symta SL (Madrid, Spain). Anycubic Photon Mono X (LCD-based SLA printer, 405 nm light source, 0.05 mm 3840 × 2400 XY resolution, 0.01 mm Z resolution, 192 mm × 120 mm ×245 mm build volume) was purchased from Anycubic® (Shenzhen, China). HPLC-grade solvents were used. All other chemicals were of reagent grade and were used without further purification.

2.2. Methods

2.2.1. Design and 3D printing of the microfluidic device

A T-shaped toroidal micromixer was designed using Tinkercad (Autodesk®, Mill Valley, CA, USA) with 3.7 cm in length, 4.7 cm in width, and 0.6 cm in height. The device featured two separated inlet channels for the entrance of the organic and aqueous phases. Each channel was 23 mm in length and 1 mm in diameter, extending up to the junction of the inlets. Following the T junction, mixing was fostered by four interconnected 5 mm diameter circular rings of 1 mm internal channel diameter connected to the outlet. The rings were aligned with a 45º . The final microfluidic chip design was exported into a standard tessellation language (.stl) digital file. This file was imported into Anycubic Photon Slicer Software (Anycubic®, Shenzhen, China). The (.stl) file was sliced to g-code format (.pwmx) for stereolithographic (SLA) printing.

The Anycubic® Photon Mono X SLA printer was used to print microfluidic devices under photopolymerization of the Anycubic® UV sensitive transparent green resin at 405 nm. The solidified resin was adhered initially to the metal platform, and the other layers adhered to this first layer, thus creating the desired object. Each layer was 0.05 mm thick. The first eight layers were exposed to UV light longer than the others (60 s) to ensure good attachment to

7

166   the metallic platform. Subsequent layers received shorter UV exposure (2 s). At the end of

167   each layer, the UV light was turned off for 1 s, preventing unwanted parts from solidifying

168   [46].

169   Once the microfluidic chip was printed, it was washed and cured using the Anycubic Wash

170   & Cure Machine 2.0 (Anycubic®, Shenzhen, China). During the washing step, the

171   microfluidic chip was immersed in isopropyl alcohol 70 % for 15 min. Subsequently, the chip

172   was removed from the isopropyl alcohol, and channels were flushed with 5 mL of ethanol.

173   Afterward, channels were flushed with 5 mL of water to ensure complete unpolymerized

174   resin removal. After the washing cycle, the chip was placed in the Anycubic Wash & Cure

175   Machine 2.0 (Anycubic®, Shenzhen, China) post-curing box for two hours under 405 nm UV

176   light. After printing, washing, and curing, the geometry of the chip was visualized with a

177   Xiaomi X3 pro phone with a 48-megapixel camera (f/1.79, 1.6-micron) (Xiaomi Inc, Beijing,

178   China).

2.2.2. Rational selection of organic solvent

180   Ethanol was selected as a suitable solvent for controlling particle precipitation due to its

181   moderate polarity with a dielectric constant of 24.55 and complete miscibility with water in

182   all proportions under normal conditions, allowing a rapid and controlled antisolvent

183   precipitation of heparin dissolved in water. Ethanol's low boiling point (~ 78 °C) is

184   advantageous for subsequent spray drying, as it readily evaporates, minimizing residual

185   solvent in the final product. Additionally, ethanol's relatively low toxicity and environmental

186   impact make it a safer choice compared to other organic solvents commonly used such as

187   dimethyl sulfoxide (DMSO) [47], aligning with green chemistry principles [48]. Its ability to

188   induce supersaturation is crucial for maintaining the integrity of macromolecules such as

189   heparin in the formulation.

2.2.3. Preparation and characterization of the microparticulate formulation

191   The aqueous phase consisted of a 50 mL solution with heparin, AZM, and leucine (75:5:20,

192   *w:w*) dissolved in deionized water (10 % *w/v*) which was loaded into a 50 mL syringe (Fisher

193   Scientific, Madrid, Spain). The composition was optimized based on a previous study [38].

194   The organic phase consisted of 50 mL of ethanol loaded in a 50 mL syringe (Fisher Scientific,

195   Madrid, Spain). Both syringes were connected to two syringe pumps (New Era Pump

196   Systems, NY, USA). Each syringe was fitted with a 14-gauge olive colour needle (with an

197   outer Ø of 1.83 mm and inner Ø of 1.75 mm) (Fisher Scientific, Madrid, Spain). One end of

198   the silicone tube (inner Ø 1.83 mm) was connected to the syringe needle outlet and the other

199   end was connected to the toroidal T-mixer's inlet cylinder tied with a cable tie to avoid

200   leakages.

201   A single batch was performed using a total flow rate of 10 mL/min and a 1:1 (*v:v*) flow ratio

202   between the aqueous and organic phases. At 14 mL intervals, a 1 mL sample was collected

203   from the outlet channel and subsequently analyzed using a Zetasizer (Malvern Instruments,

204   Malvern, UK) to evaluate mixing behaviour and assess its impact on particle size (nm), and

205   polydispersity index (PDI) (see **Figure 3**).

206   After controlled precipitation in the microfluidic mixer, the suspension containing 5 % (*w/v*)

207   solids was fed into the spray-dryer (Buchi B191 Mini Spray Dryer, Büchi Labortechnik AG,

208   Switzerland) equipped with a high-efficiency cyclone in the open mode. The process

209   parameters were set as follows: 90 °C inlet temperature, 2.5 mL/min (equivalent to 5 %)

210   solution feed rate, 800 NL/h airflow rate, and 95 % aspirator force (equivalent to 28 m³/h).

211   Under these conditions, an outlet temperature of 56 ºC ± 1 ºC was recorded. Once the solution

212   was spray-dried, the particles were collected inside the collection vessel and the following

213   three responses were evaluated: yield, AZM-loading efficiency, and encapsulation efficiency.

214   The yield was calculated by considering the difference in weight between the dry powder

215   collected after the spray drying process and the total weight of solutes (excipients and AZM)

216   introduced into the feed solution, using the following **Equation (1).**

$$\text{Yield (\%)} = \frac{\text{Weight of collected spray dried formulation}}{\text{Weight of solutes in the feed solution}} \times 100 \,\% \qquad \textbf{(1)}$$

217   High-performance liquid chromatography (HPLC) analysis was conducted using a Varian

218   Prostar 230 Solvent Delivery Module, a Varian Prostar 410 Autosampler, and a Varian

219   Prostar 310 UV-visible Detector (Varian®, Palo Alto, CA, USA). Data collection and

220   processing were performed using the Galaxie Chromatography Data System (Varian®, CA,

221   USA). AZM was separated on a Thermo Scientific BDS Hypersil C18 reverse-phase column

222   (250 mm × 4.6 mm, 5 μm). AZM was quantified using a previously validated HPLC method

223   by Al-Hakkani et al [49]. The mobile phase consisted of phosphate buffer (0.2 M KH_2PO_4,

224   pH 8): methanol (1:10 *v/v*) which was filtered through a hydrophilic 0.45 μm filter (Millipore,

225   Millex-LCR, Merck, Madrid, Spain), and pumped at a flow rate of 1.2 mL/min. The sample

226   injection volume was 50 μL. The column temperature was maintained at room temperature,

227   and the detector was set at 210 nm.

228   For drug loading (DL) and encapsulation efficiency (EE) quantification, approximately 5 mg

229   of powder formulation ($n = 3$) was weighed and dispersed in 1 mL of the mobile phase. The

230   sample was then sonicated and vortexed for 5 min before centrifugation for 5 min at 5,000

231   rpm. The supernatant was subsequently analyzed by HPLC. AZM concentrations were

232   determined by integrating the peak area at 15 min using a calibration curve. The linear

233   calibration curve range was obtained over the range of 10 μg/mL to 400 μg/mL for

234   unprocessed AZM, with an R^2 value of 0.9972 (y = 0.0918x – 2.1117). DL was calculated

235   using **Equation (2)** and EE using **Equation (3)**, both expressed as a percentage:

236
$$DL\ (\%) = \frac{\text{Weight of active ingredient}}{\text{Weight of powder formulation}} \times 100\ \% \qquad (2)$$

237
$$EE\ (\%) = \frac{\text{Total drug encapsulated}}{\text{Total drug content}} \times 100\ \% \qquad (3)$$

Numerical simulations

239   Computational fluid dynamics (CFD) simulations were performed using COMSOL

240   Multiphysics 5.6 (Burlington, MA, USA), with laminar flow and diluted species interface

241   transport. The microfluidic chip used in the experiments was consistently designed using

242   software to ensure that the experimental results closely matched the simulations. In addition,

243   the flow rates were carefully matched to the experimental setup to maintain the accuracy of

244   the comparisons [46].

245   The conservation of momentum and mass in the microfluidic chips, characterized by single-

246   phase, incompressible, and time-dependent laminar flow, was analyzed. This analysis used

247   the Navier-Stokes equations for momentum (**Equation 4**) and the continuity equation

248   (**Equation 5**) for mass conservation [50]. The equations are expressed as follows:

249
$$\rho \left(\frac{\partial \boldsymbol{u}}{\partial t} + (\boldsymbol{u} \cdot \nabla)\boldsymbol{u} \right) = -\nabla p + \mu \nabla^2 \boldsymbol{u} \qquad (4)$$

250   where (ρ) is the fluid density (kg/m³), (u) is the fluid velocity vector (m/s), (t) is time (s),

251   (p) is pressure (Pa), and (μ) is the dynamic viscosity (Pa.s).

$$\nabla \cdot \boldsymbol{u} = 0 \tag{5}$$

253   The equation implies that the fluid is incompressible [51, 52]. Solving these equations

254   provided insight into the velocity and pressure fields within the system. The resulting velocity

255   field was then used to determine the species concentration field, which was calculated using

256   the convection-diffusion equation, expressed as (**Equation 6**):

$$\frac{\partial c_i}{\partial t} + \nabla \cdot (-D_i \nabla c_i + \boldsymbol{u} c_i) = R \tag{6}$$

258   where c_i is the concentration of species (i), D_i is the diffusion coefficient (1.2×10^{-9} m²/s for

259   water–ethanol mixture), and u is the fluid velocity vector. R is the reaction rate, which was

260   assumed to be zero. The initial concentrations of the aqueous ($C_{aqueous}$), and organic ($C_{organic}$),

261   phases were set to 1 mol/m³. These standardized concentrations were applied at their

262   respective inlets to bind the concentration fields accurately for the dilute species transport

263   analysis.

264   The density of water (ρ_{water}) was 997 kg/m³; the density of ethanol ($\rho_{ethanol}$) was 789 kg/m³;

265   the viscosity of water (μ_{water}) was 0.001 Pa s and the viscosity of ethanol ($\mu_{ethanol}$) was 0.0012

266   Pa s [53].

267   Analyzing homogeneity at the outlet of the microfluidic chip is one method used to assess

268   mixing. The statistical measure of uniformity in the mixed solutions was determined by

269   calculating the standard deviation of the concentration. Previous studies [51, 52, 54] have

270   used methods based on the standard deviation of concentration to assess the mixing in

271   microfluidic chips. In this study, the efficacy (M) was calculated using a formula derived

272   from the standard deviation of concentration, which is expressed as follows (**Equation 7**):

$$M = 1 - \frac{\sigma}{\sigma_{Max}} \tag{7}$$

274   where, σ represents the standard deviation of species concentration at a given cross-section,

275   while σ_{Max} indicates the standard deviation in a completely unmixed state. The efficacy,

276 indicated as 'M', is quantified on a scale where 0 corresponds to the unmixed state and 1 to a
277 fully mixed state. The standard deviation was calculated as follows (**Equation 8**):

$$\sigma = \sqrt{\frac{1}{N}\sum_{i=1}^{N}(c_i - c_m)^2} \qquad \textbf{(8)}$$

279 where N is the number of sampling points, c_i is the mixing fraction at point (i), c_m is the
280 optimal mixing fraction.

Morphology and particle size characterization

282 The mean particle size after dispersion in aqueous media (5 mg/mL), polydispersity, and zeta
283 potential were measured using a Zetasizer (Malvern Instruments, Malvern, UK). This
284 concentration was optimised in previous studies [55]. Measurements of mean particle size
285 and polydispersity were performed at a scattering angle of 90º and a temperature of 25 ºC.
286 Before measurements, polystyrene standards (diameter = 100 nm) were measured; size
287 results were in accordance with the nominal size of the standard particles [56].

288 Transmission Electron Microscope (TEM) (JEM 1400 plus JEOL, Japan) equipped with an
289 acceleration voltage ranging from 40 kV to 120 kV was used for imaging. A drop of an
290 aqueous sample dispersion (5 mg/mL) was placed onto a Formvar/carbon-coated grid, and
291 the excess sample was blotted off with the Whatman Nº 1 filter paper. The samples were then
292 negatively stained with 1 % *w/v* phosphotungstic acid solution. Images were captured using
293 an AMT digital camera [57].

2.2.4. Solid state characterization

Morphology

296 The morphology of the optimized microparticulate formulations after spray drying was
297 characterized by Scanning Electron Microscopy (SEM) (JSM 6335F JEOL, Japan) equipped
298 with a secondary electron detector at 15 kV. Samples were sputter coated with pure gold
299 using a metallizer (Q150RS Metalizador QUORUM, Quorum Technologies Ltd., Lewes,
300 UK) for 180 s under vacuum. Particle sizes were measured using ImageJ software version
301 1.53t (National Institutes of Health, USA)

Powder X-Ray Diffraction (pRXD)

303   Powder X-ray analysis was conducted using a Philips®X'Pert-MPD X-ray diffractometer

304   (Malvern Panalytical®; Almelo, The Netherlands) equipped with Ni-filtered Cu K radiation

305   (1.54). The study was performed at 40 kV voltage and 40 mA. PXRD patterns were recorded

306   at a step scan rate of 0.05°/s, ranging from 5° to 40° on the 2-theta scale ($n = 3$). For

307   comparison purposes, physical mixtures of raw powder materials between API and

308   excipients, prepared in an agate mortar and pestle were used [19].

309   **Fourier-Transform Infrared (FTIR) Spectroscopy**

310   FTIR analysis was performed using a Nicolet Nexus 670–870 (Thermofisher, Madrid,

311   Spain). A wavelength range between 400 cm^{-1} – 4000 cm^{-1} was used with a 1 nm step scan.

312   Spectra were interpreted using Spectragryph (version 1.2.9, Oberstdorf, Germany) software,

313   and data normalization was carried out.

314   **Differential Scanning Calorimetry (DSC) coupled with Thermogravimetric Analysis**

315   **(TGA)**

316   DSC-TGA standard scans were conducted using 5-6 mg weight powder with nitrogen as the

317   purge gas on an SDT Q600 instrument (TA instruments, Elstree, UK) calorimeter. A

318   scanning rate of 10 °C/min was used from 25 °C to 350 °C. The instrument was calibrated

319   using indium as the standard. The glass transition temperatures reported are the midpoint of

320   the transition ($n = 3$) [58].

321   **2.2.5.** *In vitro* **Haemolysis Assay**

322   Haemolysis studies were performed with red blood cells (RBCs) to assess the toxicity of the

323   formulation. Cells were obtained from the blood of a healthy 28-year-old male volunteer,

324   following ethical procedures approved by Universidad Complutense de Madrid (Madrid,

325   Spain) in EDTA coated Vacutainers® (K2-EDTA, BD Vacutainer® tubes, Becton Dickinson

326   and Co., New Jersey, USA). The blood was centrifuged at 3,000 rpm for 5 min, and

327   hematocrit, and plasma levels were marked on the tube. The supernatant (plasma) was

328   removed, and the erythrocytes were washed three times with an equivalent volume of 0.9 %

329   NaCl (150 mM), followed by centrifugation at 3,000 rpm for 5 min at each step. After

330   washing, the supernatant was discarded, and the RBCs were resuspended in PBS pH 7.4 to a

331   final concentration of 4 % *w/w*. Subsequently, a volume of 180 µL was added to each well

332 [59]. Samples (microparticles, excipients, and APIs) were dispersed with PBS (1X, pH 7.4)

333 to produce 8 serial dilutions of AZM concentration ranging from 200 µg/mL to 1.65 µg/mL

334 (20 µL, *n=3*). Triton® X-100 (Sigma-Aldrich CO, St. Louis, USA) in PBS (1X, pH 7.4)

335 prepared at 20% *w/v* or PBS (1X, pH 7.4) were used as a positive and negative control (20

336 µL) respectively. The plates were then incubated at 37 ºC for 1 h (Memmert GmBH + Co.,

337 Schwabach, Germany). Subsequently, the plates were centrifuged at 1,500 rpm for 5 min to

338 pellet intact erythrocytes. The supernatant (100 µL) was transferred to a clear flat-bottomed

339 96-well plate. Absorbance (ABS) was measured at 570 nm using a plate reader (BioTeK,

340 EKx808). The percentage of haemolysis was calculated using the **Equation (9)**:

341
$$\% \, Haemolysis = \frac{ABS1 - ABS2}{ABS3 - ABS2} \, 100 \tag{9}$$

342 where ABS1 sample represents the absorbance of the sample, ABS2 is the absorbance of the

343 negative control, and ABS3 is the absorbance of the positive control. The concentration

344 needed to produce 50 % haemolysis (HC$_{50}$) was calculated using Compusyn™ v1.0

345 (Combosyn Inc., New Jersey, USA).

346   2.2.6.   Antibacterial *in vitro* disk diffusion assay

347 The antibacterial effect of the loaded microparticles was tested against *Haemophilus*

348 *influenzae* (CECT 8452). The antimicrobial activity was tested by Diagnostic Sensitivity Test

349 (DST) with a chocolate horse blood agar plate (Oxoid™, Thermo Scientific, Madrid, Spain).

350 AZM-loaded microparticles dispersed in deionized water (23 mg/mL equivalent to 0.75

351 mg/ml of AZM) were loaded (20 µl) onto 6 mm in diameter paper disks and placed in the

352 center of agar plates (corresponding to a final AZM dose of 15 µg onto each paper disk).

353 Commercial disks of AZM (15 µg, Oxoid™, Thermo Scientific, Basingstoke, UK) were used

354 as a control. Inhibition zone diameters were measured with a caliper (Cole Parmer, Fisher

355 Scientific, Madrid, Spain) at points where there was complete inhibition of bacterial growth

356 after 24 h of incubation. Isolates were classified as AZM susceptible (S) when the zone of

357 inhibition was greater than $\geq$ 12 mm according to the National Committee for Clinical

358 Laboratory Standards (NCCLS) [60].

359   2.2.7.   *In vitro* Lung Deposition

360   A Next Generation Impactor (NGI; MSP Corporation, Shoreview, USA), connected to an

361   HCP5 vacuum pump (Copley Scientific, Nottingham, UK) through a critical flow controller

362   (TPK 2000 Copley Scientific, Nottingham, UK) was used. The NGI apparatus comprised

363   seven stainless compartments (stages), a stainless-steel induction port, and one micro-orifice

364   collector (MOC). To ensure accurate analysis and prevent particle bouncing, the cups of the

365   impactor were coated with a solution of 2 % (*w/v*) Tween 20 in ethanol and led the solvent to

366   evaporate before use. Airflow of 30 L/min and 60 L/min was set using a TSI 4,000 series

367   Mass Flow Meter 4040 (TSI Incorporated, Shoreview, USA), with an inhalation time of 8 s

368   and 4 s and a total inhaled air volume of 4 L. For the aerosolization, a hydroxypropyl

369   methylcellulose capsule (No. 3) filled with 25 mg $\pm$ 1 mg of formulation (*n* = 3) was placed

370   in a Handinhaler (Boehringer, Ingelheim am Rhein, Germany) device. The formulations

371   deposited in each part of the NGI were quantified using the previously described HPLC

372   method. The mass median aerodynamic diameter (MMAD) and fine particle fraction (FPF)

373   (<3 µm and <5 µm) were calculated to evaluate the *in vitro* deposition of the tested

374   formulations. MMAD was calculated by plotting cumulative particle mass percentage versus

375   aerodynamic diameter on log-probability paper using all NGI stages. FPF values were

376   expressed as a fraction of the emitted dose, calculated based on the AZM mass deposited on

377   impactor stages relative to the total emitted dose [55]. Stage cut-off diameters were

378   determined according to Marple et al. (2003) [61].

379   *2.2.9. In vitro* **cell culture assays**

380   **Cell Culture Conditions**

381   Human bronchial epithelial Calu-3 cells, obtained from ATCC (No. HTB-55, Lot. 61449062),

382   were cultured in DMEM/F-12 with glutamine supplemented with 10 % Fetal Bovine Serum

383   (FBS) and 1 % penicillin/streptomycin. Murine macrophage J774A.1 cells (ATCC® TIB-

384   67™) were cultured in RPMI-1640 medium supplemented with 10 % FBS and 1 %

385   penicillin/streptomycin. The cells were maintained at 37 ºC in a humidified incubator with 5

386   % CO_2.

387   **Cell Viability Assay**

388   MTT assay was used to assess cell viability. Cells were seeded in 96-well culture plates at a

389   density of 3.0×10^4 cells per well (Calu-3 cells) and 1.0×10^4 cells per well (J774A.1 cells).

390   Cells were treated with different concentrations of AZM ranging from 0.10 μg/mL to 50

391   μg/mL for 24 h. Triton-X solution (5 %) was used as a positive cytotoxic control. MTT

392   solution (5 mg/mL) was added (100 μL), and cells were incubated for 4 h in the darkness.

393   Formed formazan crystals were then dissolved in isopropyl alcohol (Calu-3 cells) or DMSO

394   (J774A.1 cells). Absorbance was measured at 550 nm using a Spectrostar BMG microplate

395   reader (BMG LABTECH, Ortenberg, Germany). The percentage of viable cells was

396   calculated using untreated cells as control, being considered as 100 % cell viability. MTT

397   assays were done in triplicate.

398   **2.2.8. Statistical Analysis**

399   Statistical analysis was performed via a one-way ANOVA test using Minitab v.19 (Minitab

400   Ltd., Coventry, UK) followed by Tukey's test (95 % level of significance). The results were

401   plotted using Origin 2021 (OriginLab Corporation, Northampton, MA, USA).

402   **3. Results**

403   **3.1. Microfluidic device characterization**

404   **Figure 1A-B** displays the computer-aided design (CAD) of the 3D printed microfluidic

405   device fabricated using SLA technology, along with the final prototype, showcasing the

406   successfully printed model and detailing the dimensions of the internal channels. The

407   dimensions of the 3D-printed device matched closely with those in the design. Channels were

408   opened after appropriate flushing with ethanol and water.

409
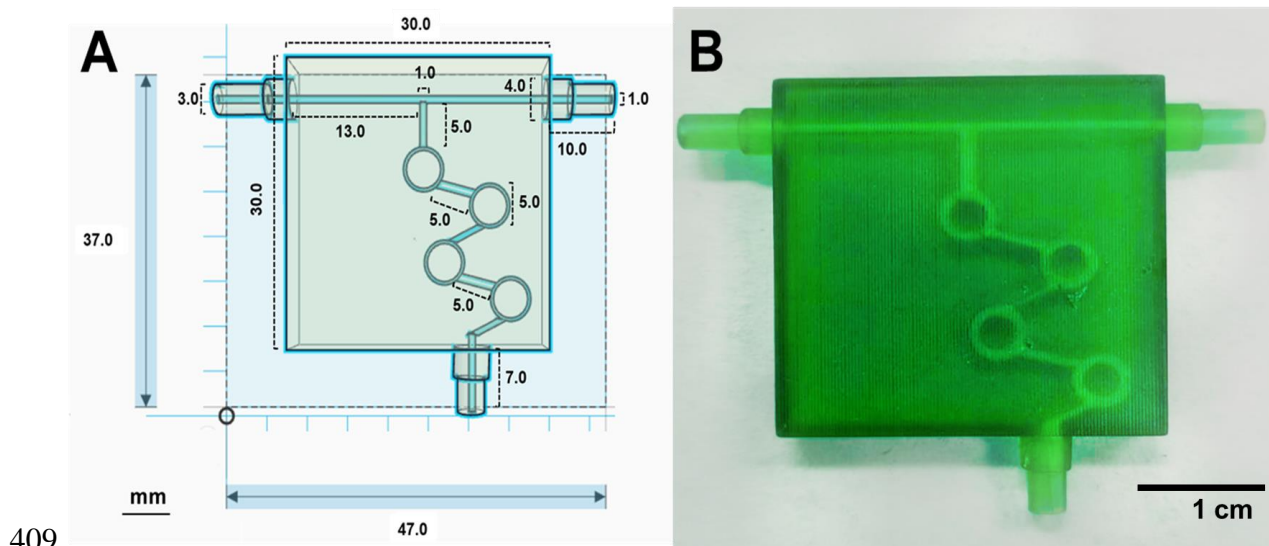
410   **Figure 1. Design and 3D printed microfluidic device**. Key: **(A)** Geometrical design and dimensions of the

411   3D microfluidic device, **(B)** 3D printed microfluidic device by SLA. Photograph obtained from a Xiaomi X3

412   pro phone (Xiaomi Inc, Beijing, China).

413   **Figure 2** illustrates the changes in velocity, pressure, and aqueous phase concentrations

414   during mixing within the microfluidic chip simulations using COMSOL. The velocity

415   reached up to 0.3 m/s, with the fluids primarily interacting at the intersections of the circular

416   sections. The pressure gradually decreased towards the outlet, indicating that most of the

417   mixing occurred at these intersections, with only a small portion extending into the circular

418   regions. The concentration field of the aqueous phase, where the API is located, demonstrates

419   that despite a higher concentration at the intersections, the overall mixing within the

420   microfluidic device was homogeneous and nearly fully mixed. This can be seen in Figure

421   2C, where the outlet concentration is closer to 0.5 - indicating a balanced mixture - compared

422   to 1, which would indicate only the aqueous phase, and 0, which would indicate only the

423   organic phase.

424
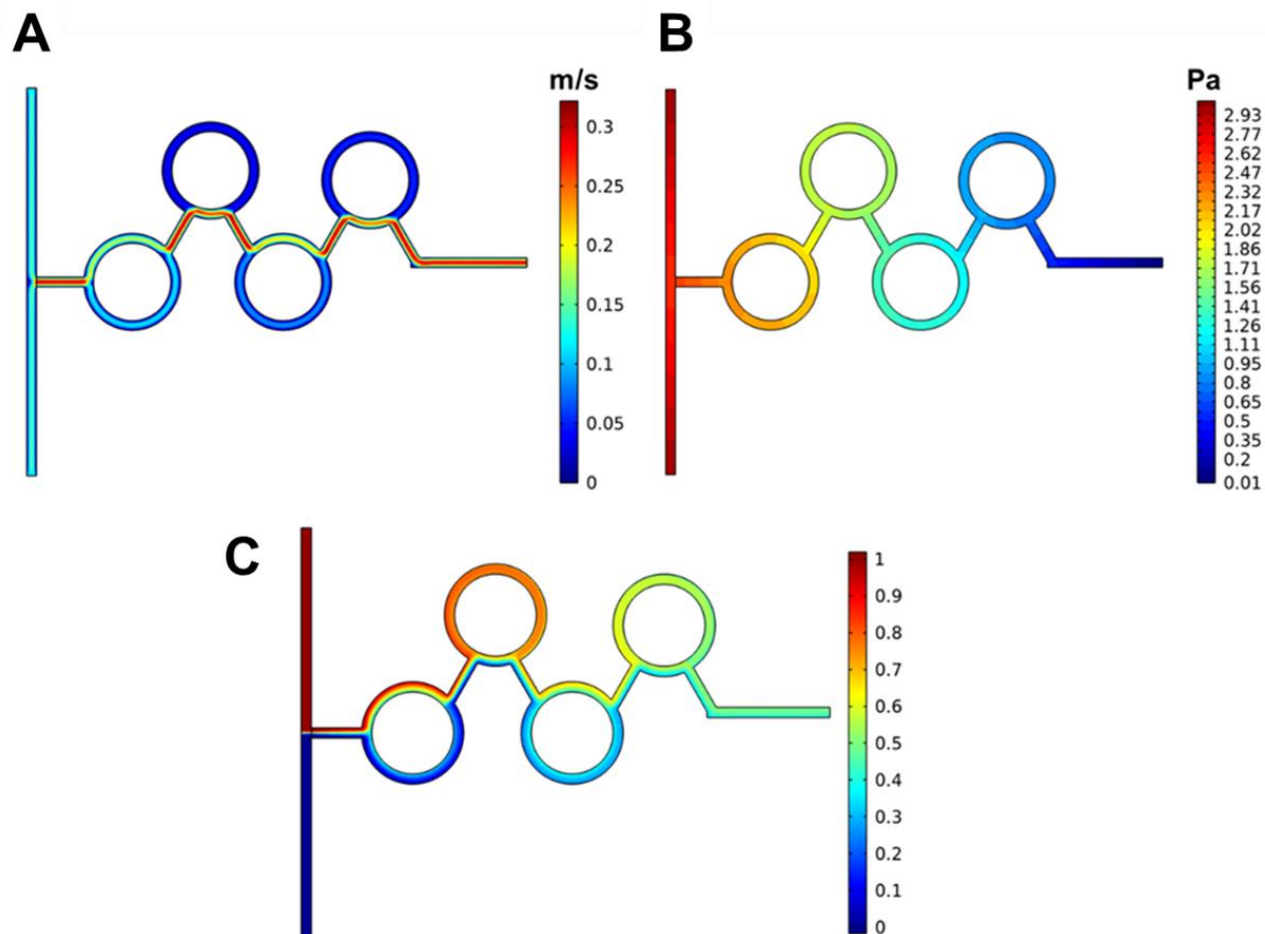
Figure 2. **Contours of mixing in the microfluidic chip after 2 seconds**. Key: (**A**) velocity magnitude (m/s), (**B**) Pressure (Pa), (**C**) Concentration field of the aqueous phase during the mixing period where close to 1 shows unmixed state and 0.5 homogeneously mixed state.

This result aligns with the calculated mixing index (M) of approximately 0.943, where a value of 1 indicates a fully mixed state and 0 indicates no mixing. These results indicate a high level of mixing efficiency within the microfluidic chip, supporting the effectiveness of the design used in this study.

The microfluidic mixing process enables the consistent production of nanoprecipitates with controlled size distributions (Figure 3, Table S1). Particle size was measured at different time points throughout a 100 mL mixing cycle, with an average size of 170 nm. Across most time points, particle sizes remained within a ± 20% variability range, except for the final measurement. This deviation is likely due to reduced mixing efficiency caused by poorer liquid dispensing control when only a minimal fluid volume remained in the syringe pump.

438   In contrast, the polydispersity index (PDI) exhibited a significant linear decline throughout

439   the cycle, indicating increasingly homogeneous particle distribution.
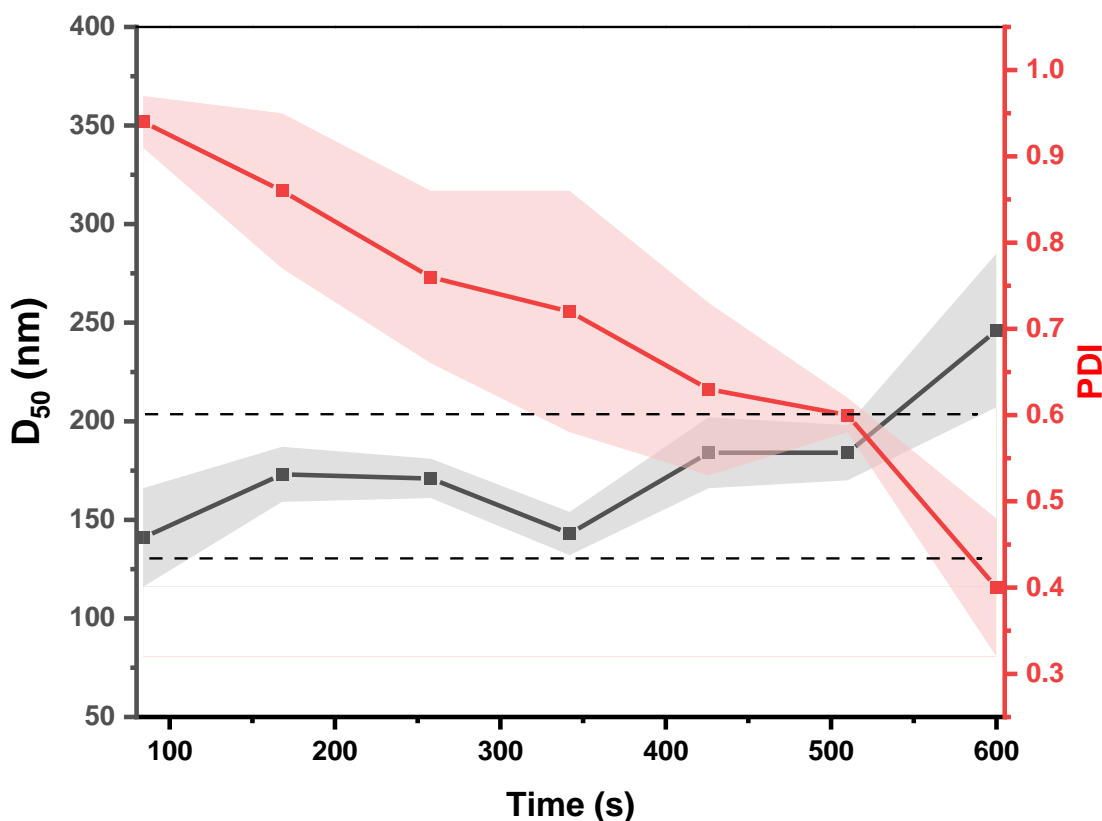
440

441   **Figure 3**. Impact of the mixing process within the micromixer on particle size (D_{50}) and polydispersity (PDI).

442   Data are expressed as mean ± SD *(n = 3)*. Particle size is expressed in number (D_{50}, nm). The shadowed area

443   corresponds to the SD. Dashed lines represent the average D_{50} ± 20% variability.

444   **3.2. Microparticle characterization**

445   After the spray drying process, the yield obtained in the formulation was 57.0 % ± 6.3 %.

446   The DL of AZM within the microparticles was 3.3 % ± 0.5 %, and the EE was 66.6 % ± 10.6

447   %. Upon reconstitution in aqueous media, the mean particle size was 461.6 nm ± 38.4 nm

448   and particles showed a negative zeta potential of -19.2 mV ± 4.5 mV indicating good

449   colloidal stability.

450   The morphology of AZM-loaded microparticles is illustrated in **Figure 4**. The SEM

451   micrographs revealed a homogeneous appearance with particle sizes around 1 µm (**Figure**

452   **4A**). No presence of AZM or leucine crystals was detected at the surface of the microparticle

453   indicating an optimal drug encapsulation which was also corroborated by X-ray analysis

454   (**Figure 5**). Electron-dense particles < 1 µm in size were observed using TEM (**Figure 4B**).

455   The core of the particles showed an intricated fibril mesh which can be attributed to the ionic

456   complexation occurring between heparin and AZM during the controlled precipitation within

457   the micromixer.
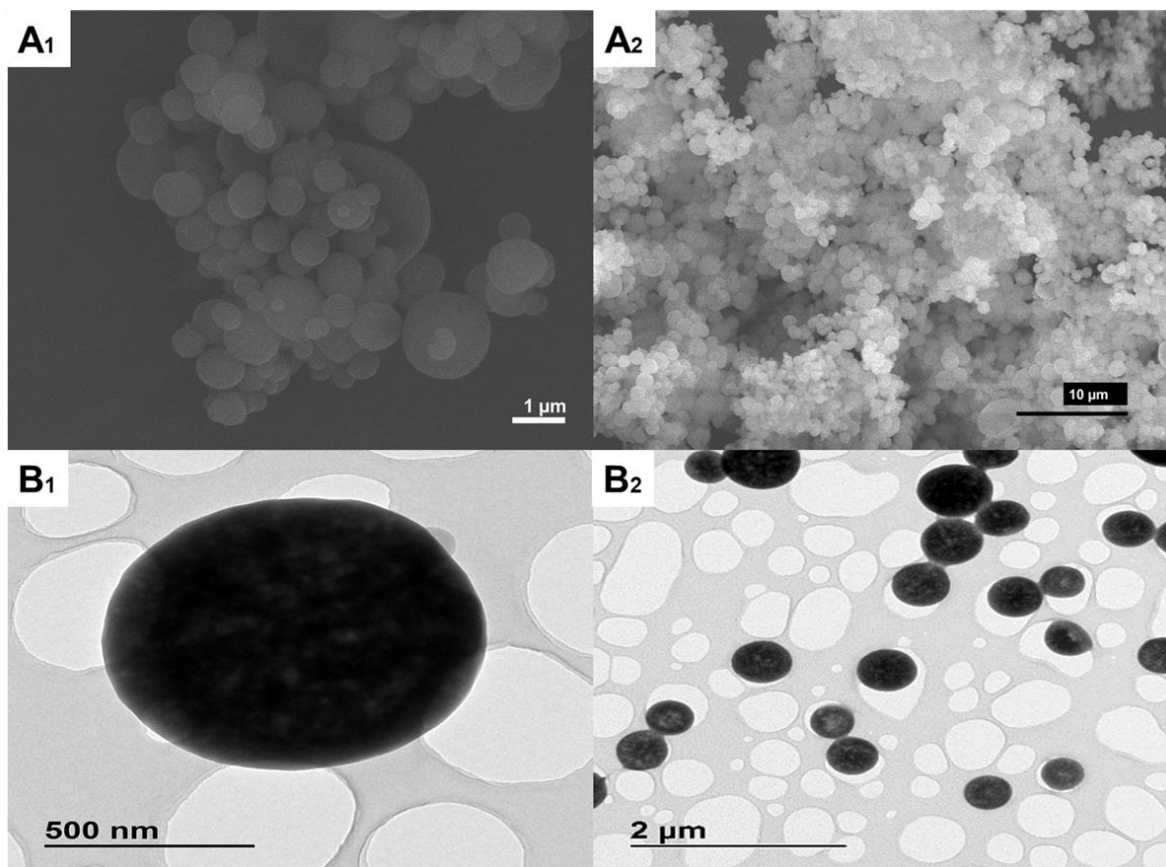
458

459   **Figure 4. Morphological analysis.** SEM and TEM micrographs were obtained at different magnifications**.**
460   Key: **A)** SEM and **B)** TEM.

461   **3.3. Solid state characterization of the microparticle formulation**

462   **PRXD analysis**

463   PXRD analysis showed distinct Bragg peaks for unprocessed AZM and leucine indicating

464   their crystalline structure while unprocessed heparin exhibited an amorphous halo (**Figure**

465   **5**). Peaks of leucine and AZM were still present in the physical mixture. However, the

466   microparticle formulation exhibited a completely amorphous halo, suggesting that the spray-

467   drying process induced full amorphization.
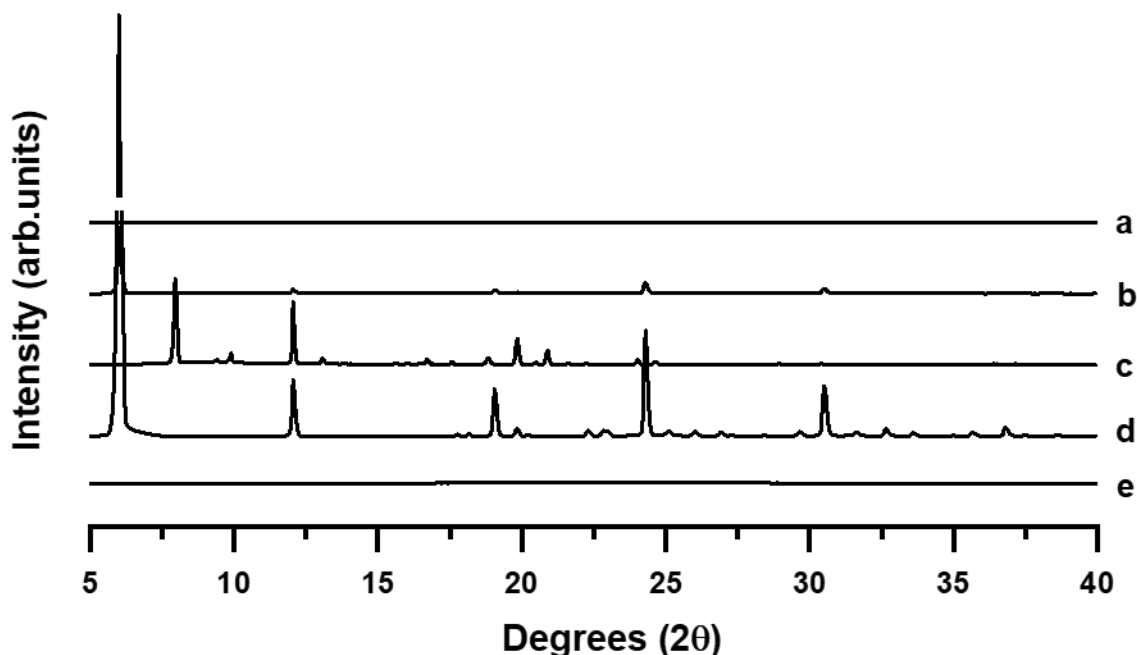
468

469

470 **Figure 5. PXRD analysis**. Key: **(a)** Microparticles, **(b)** Physical mixture, **(c)** Unprocessed AZM, **(d)**
471 Unprocessed Leucine, and **(e)** Unprocessed Heparin.

472 **FT-IR analysis**

473 FTIR analysis revealed clear differences between the physical mixture and the microparticles
474 after the spray-dried process (**Figure 6**). The physical mixture showed a combined spectral
475 pattern of the individual components, indicating minimal interaction. However, the
476 microparticle formulation exhibited significant peak shifts and intensity changes, particularly
477 in the 1700 cm^{-1} - 1500 cm^{-1} region, suggesting H-bond interactions and electrostatic
478 interactions, formed during the nanoprecipitation. In the region between 1300-1000, well-
479 defined and sharper peaks were observed for the microparticulate formulation compared to
480 the unprocessed heparin which can be attributed to differences in particle size [62].
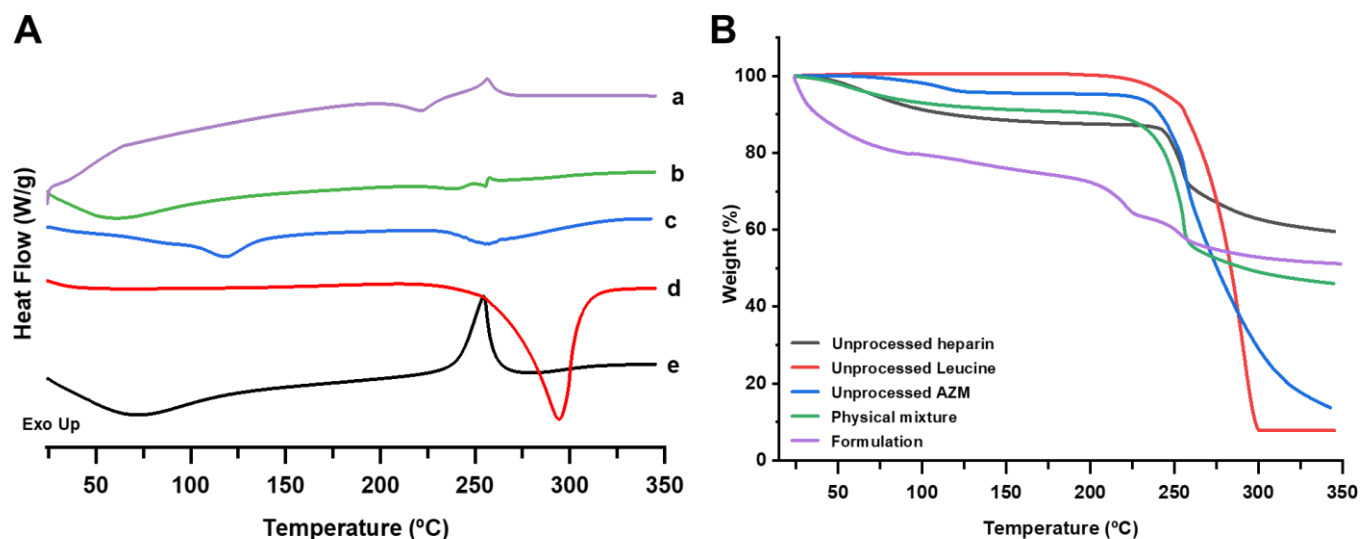
481
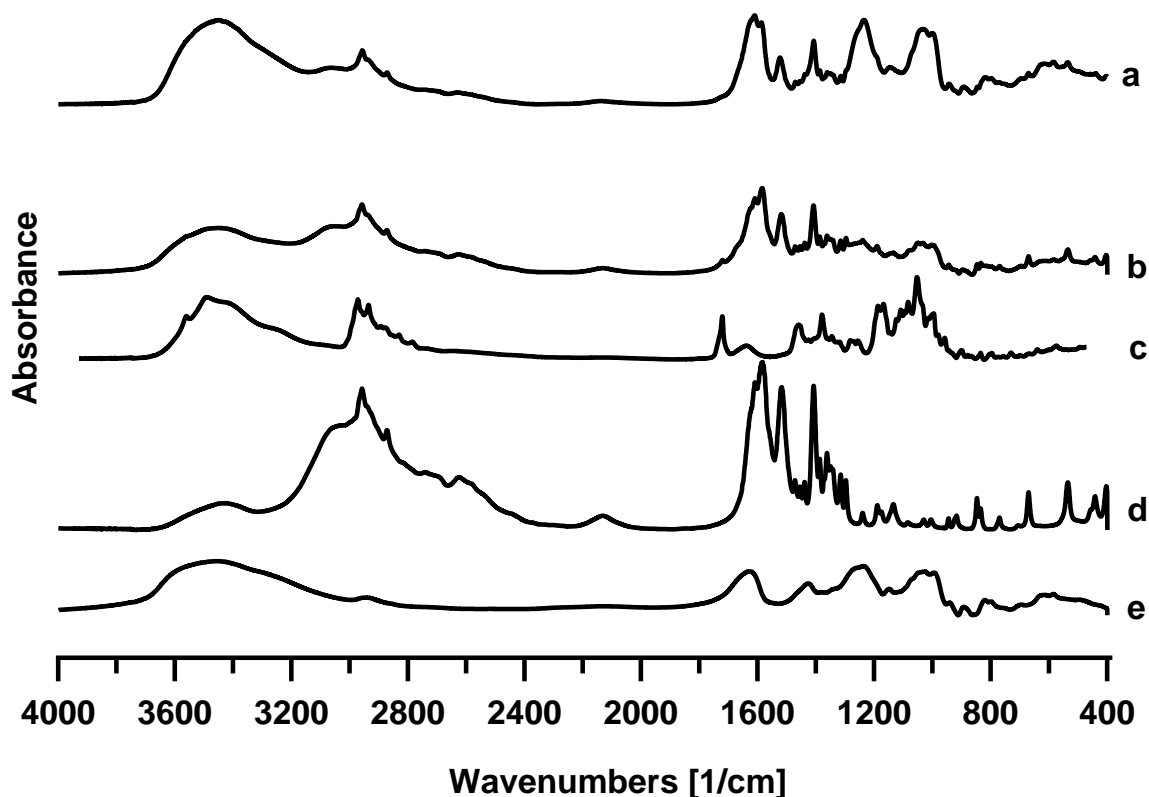
Figure 6. FTIR analysis. Key: **(a)** Microparticles, **(b)** Physical mixture, **(c)** Unprocessed AZM, **(d)** Unprocessed Leucine, and **(e)** Unprocessed Heparin.

DSC-TGA analysis

Thermal analysis for the formulation and unprocessed materials is shown in **Figure 7**. Unprocessed leucine showed a characteristic melting event at 287 °C ± 1 °C as well as the azithromycin at 120 °C ± 1 °C. Unprocessed heparin showed a thermal degradation above 250 °C. DSC analysis of the microparticulate formulation demonstrated the absence of endothermic peaks which can be correlated with its amorphous nature (**Figure 7A**). The TGA analysis revealed that the microparticulate formulation underwent a rapid initial weight loss (~20 %) up to 100 °C, attributable to the evaporation of residual solvents after the spray-drying process (**Figure 7B**). The microparticulate formulation also exhibited lower thermal stability compared to the physical mixture, starting to degrade from 200 °C onwards.

494

495

**Figure 7. DSC-TGA analysis. (A)** DSC and **(B)** TGA. Key: **(a)** Microparticles, **(b)** Physical mixture, **(c)** Unprocessed AZM, **(d)** Unprocessed Leucine, and **(e)** Unprocessed Heparin.

3.4. *In vitro* assessment of aerodynamic performance

The *in vitro* deposition profile of the formulation is shown in **Figure 8** and summarized in **Table 1**. While the MMAD was equivalent at both inspiratory flows, the aerodynamic performance analysis of the DPI formulation revealed distinctive deposition patterns across different flow rates. The FPF < 5 μm achieved at 30 L/min (57.2 % ± 7.4 %) was significantly higher compared to 60 L/min (47.9 % ± 1.3 %), suggesting superior powder dispersion characteristics at lower inspiratory flow rates.

Table 1. FPF below 5 μm and 3 μm at 30 L/min and 60 L/min for 8 and 4 s. Data are expressed as mean ± SD (*n = 3*). Key: MMAD, Mean Mass Aerodynamic Diameter.

| Air flow	FPF < 5 μm (%)	FPF < 3 μm (%)	MMAD (μm)
30 L/min	57.2 ± 7.4	45.8 ± 5.9	4.0 ± 1.0
60 L/min	47.9 ± 1.3	32.8 ± 0.4	4.1 ± 0.1

507
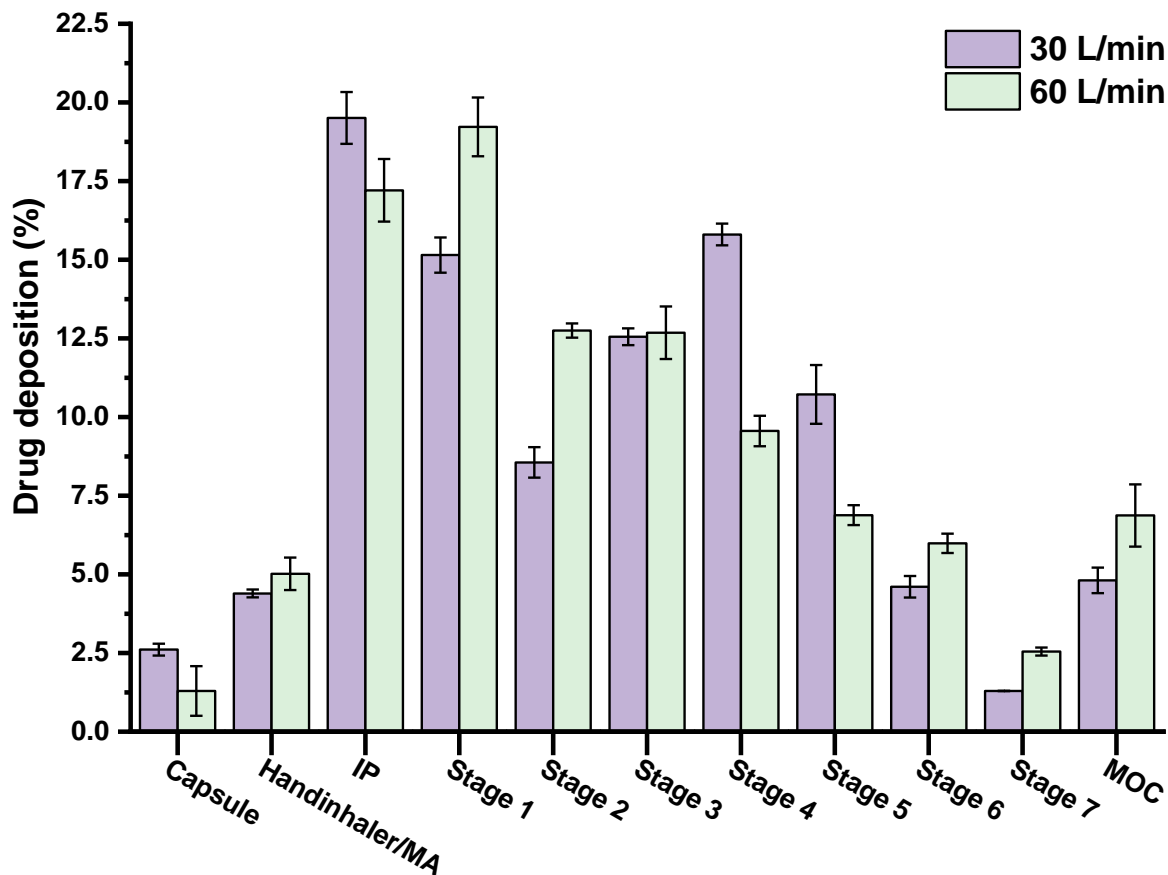
Figure 8. *In vitro* **deposition of AZM in different stages of the NGI. Key**: (**Handinhaler/MA**) device + mouth adaptor (**IP**) induction port), and (**MOC**) micro-orifice collector.

3.5. *Ex vivo* haemolysis and antibacterial *in vitro* assay

Ex vivo haemolysis on human RBCs (**Figure 9A**) exhibited significantly lower haemolytic toxicity for the AZM-loaded microparticle formulation compared to unprocessed AZM within all the tested concentrations. This difference indicates that the encapsulation of AZM within heparin microparticles substantially reduced its haemolytic toxicity. The HC_{50} for the microparticle formulation was 126-fold higher than unprocessed AZM indicating an optimal safety profile.

Antibacterial efficacy studies against *H. influenzae* demonstrated equivalent inhibitory activity for the AZM-loaded microparticles compared to the standard (**Figure 9B**). The formulation exhibited an inhibition halo of 21.13 mm ± 0.38 mm, which was comparable to that of the commercial AZM disk (21.00 mm ± 0.56 mm). No statistical significance ($p >$

521 0.05) was observed, indicating that the AZM-microparticles formulation maintained
522 antimicrobial efficacy being able to diffuse from the carrier.

523
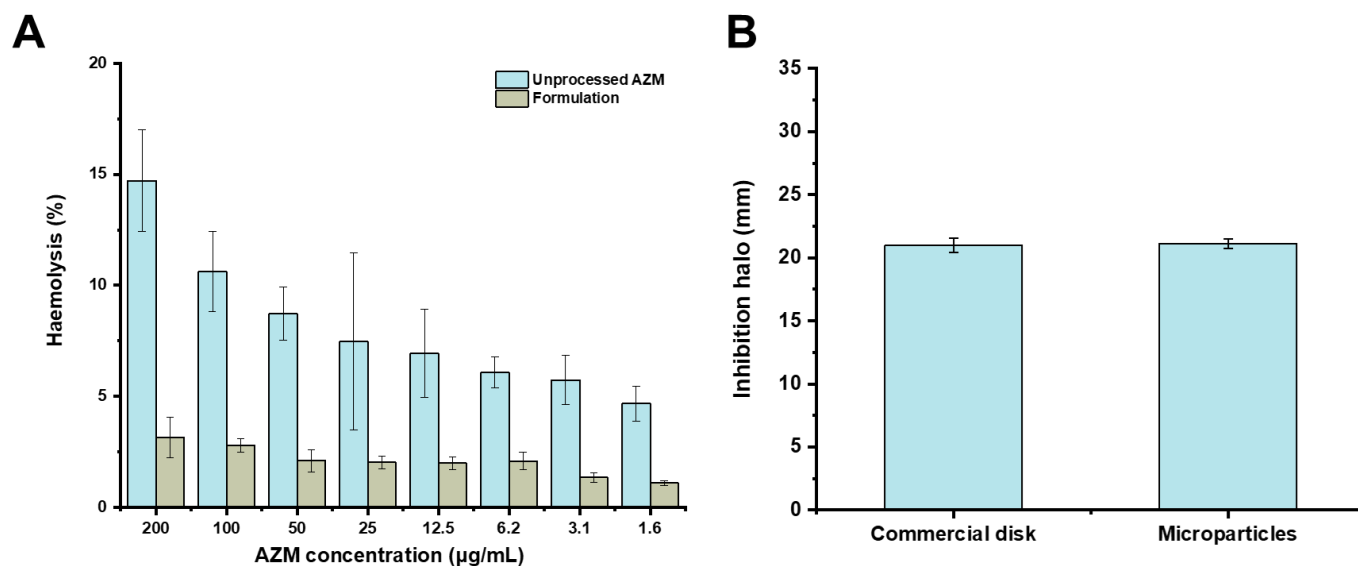
Figure 9. **A)** *In vitro* **haemolysis of AZM-loaded microparticle formulation.** Data are expressed as mean ±
SD (*n = 3*). **B)** *In vitro* **antibacterial assay against** *H. influenzae***.** Data are expressed as mean ± SD (*n* = 5).

3.6. *In vitro* cytotoxicity MTT assays

Figure 10 shows the effect of the AZM-loaded microparticles on Calu-3 and J774A.1 cell
viability. In Calu-3 cells, cell viability remained high (> 94 %) at concentrations up to 25
µg/mL, indicating a favorable safety profile and minimal cytotoxicity. However, a moderate
but significant decrease in cell viability was observed at the highest tested concentration of
50 µg/mL, reducing viability to 64.5 % (**Figure 10A**). Microscopic examination supported
these findings, revealing minimal morphological alterations at 25 µg/mL, while pronounced
morphological changes and a reduction in cell number were observed after incubation with
50 µg/mL AZM-loaded microparticles. (**Figure 10C**). On the other hand, the AZM
formulation had no effect on the viability of J774A.1 cells at any assayed concentrations
(from 0.1 to 50 µg/mL) (**Figure 10B**).

Calu-3 cell morphology
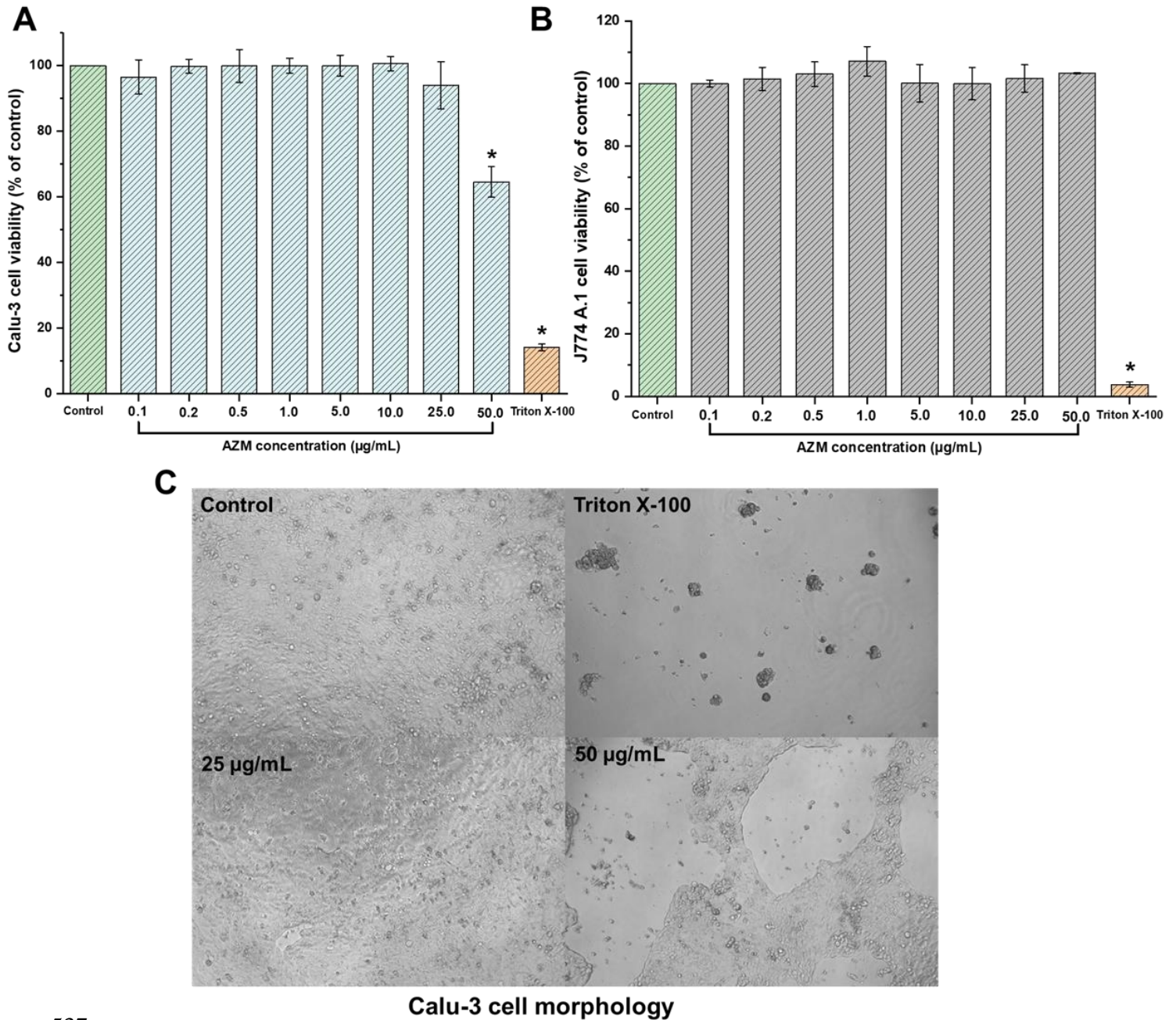
537

538   **Figure 10. Effect on cell viability using MTT assay. A)** Calu-3 cells, and **B)** J774A.1 cells. Cells were treated

539   with the formulation at AZM concentrations ranging from 0.1 µg/mL to 50.0 µg/mL for 24 h. Triton X-100 was

540   used as a positive cytotoxic control. Data are expressed as mean ± SD ($n = 6$). ***$p < 0.05$** *vs* control. **C) Effect**

541   **on Calu-3 cell morphology.** Images were obtained with a Leica microscope at x10 magnification at 25 µg/mL

542   and 50 µg/mL AZM concentration at 24 h.

543   **Discussion**

544   The integration of microfluidics with spray drying has shown to be a promising approach for
545   the manufacture of inhalable microparticles. This process enables the continuous
546   manufacture of dry powder inhalers which, to the best of our knowledge, has not been
547   previously described. This approach has the potential to revolutionize the current landscape
548   of industrial strategies for fabricating dry powder inhalers. The integration of microfluidics
549   allows for precisely controlled precipitation making it easier to tune the desired particle size
550   while the spray-drying ensures a suitable drying step preventing aggregation.

551   Microfluidic micromixers have been previously used for drug nanoencapsulation using
552   carbohydrates. Tran *et al.* (2012) [63] developed a microfluidic chip that rapidly synthesized
553   uniform heparin-folic acid-retinoic acid nanoparticles (130 nm, PDI = 0.101) with high drug
554   coupling ratios (17 drug molecules per heparin chain) via ionic complexation. The
555   microfluidic chip was designed with a solvent-resistant fluoropolymer, forming a 500 µm
556   wide, 50 µm high, and 40 cm long microchannel with two inlets and one outlet. This
557   geometry enabled precise control over reagent mixing and residence time, facilitating
558   efficient drug conjugation to heparin chains. Flow rates were adjusted to control reaction
559   time using a dual syringe pump, solutions were introduced at identical flow rates, achieving
560   residence times of 1 to 2.5 min. The microfluidic approach significantly reduced the reaction
561   time from days to minutes compared to bulk synthesis. The nanoparticles produced by the
562   microfluidic chip exhibited a 37 % increase in cellular uptake with a 20 % increase in
563   cytotoxicity against cancer cells compared to their bulk-synthesized counterparts.

564   In our work, the microfluidic design was optimized based on CFD simulations along with
565   experimental validation to enhance mixing efficiency and particle engineering. The T-
566   junction was selected to ensure rapid initial contact between the organic and aqueous phases,
567   promoting early-stage diffusion and minimizing phase separation. The four interconnected
568   circular rings (5 mm diameter, 1 mm channel width) positioned at a 45º angle were designed
569   to induce chaotic advection, which is crucial for efficient mixing in laminar flow regimes.
570   The 1 mm channel diameter was chosen to balance flow resistance and Reynolds number,
571   ensuring effective mixing while maintaining a manageable pressure drop. The overall
572   dimensions (3.7 cm × 4.7 cm × 0.6 cm) were constrained by the resolution and build volume
573   of the 3D printer while ensuring practical handling and integration with fluidic connections.

574   These design choices significantly impact particle quality by reducing concentration
575   gradients, controlling shear rates, and preventing aggregation, ultimately leading to uniform
576   and well-defined particles.

577   The geometry of the microfluidic micromixer was optimised to achieve an enhanced mixing
578   index of 0.943 which combined with a low total flow rate (10 mL/min), a larger particle size
579   for optimal lung delivery was targeted. Ionic complexation is also expected to occur during
580   the controlled precipitation step considering that at physiological pH, heparin is negatively
581   charged while AZM is the opposite. The coupling with spray drying resulted in a high yield
582   (57 %), DL (3.3 %) and EE (66 %) considering the hydrophilic nature of the drug. Previous
583   reports on AZM encapsulation exhibited much lower yields and EE (< 50 %) [64, 65]. Also,
584   particles obtained by combining the nanoprecipitation within the micromixer with the spray
585   drying resulted in a smaller size with a more homogenous particle size distribution with
586   greater deposition in the lungs compared to direct spray drying [66].

587   DPI performance is influenced by device resistance, which determines the relationship
588   between inspiratory pressure and flow rate. Higher-resistance DPIs result in lower flow rates
589   at the same inspiratory effort, affecting aerosolization and deposition efficiency. The
590   Handihaler device, for example, delivers dry powder at flow rates as low as 20 L/min. In
591   COPD patients with severely compromised lung function (correlated with a mean Forced
592   Expiratory Volume in 1 second of 1.02 L), the median peak inspiratory flow through the
593   Handihaler was 30.0 L/min (range 20.4–45.6 L/min) [67]. These findings align with data
594   showing that at a lower flow rate of 30 L/min, fine particle fractions (FPF < 5 μm: 57.2% $\pm$
595   7.4%; FPF < 3 μm: 45.8% $\pm$ 5.9%) suggest improved deep lung deposition, particularly in
596   the alveolar region due to enhanced diffusion. This is crucial for patients with reduced
597   inspiratory capacity, such as those with COPD or asthma, as lower flow rates enhance
598   gravitational settling and minimize exhalation losses. Given the variability in drug delivery
599   based on inspiratory flow, optimizing inhaler design for patients with compromised
600   respiratory function remains essential [68, 69].

601   A significant advantage of this formulation is its lower susceptibility to inspiratory flow rates
602   compared to other formulations [70-72]. No significant differences were observed in the
603   MMAD but a greater FPF was obtained for the lower inspiratory airflow tested. The

28

604   integration of microfluidic technology with spray drying allows for the precise control of

605   droplet formation, which is essential for achieving uniform and smaller particle sizes suitable

606   for alveolar deposition ($< 3\ \mu$m) [73].

607   Particle size plays a critical role in determining the deposition, distribution, and efficacy of

608   drugs delivered to the lungs. Particles smaller than 5 µm, particularly those between 0.5 µm

609   - 2 µm, are ideal for achieving optimal lung deposition and alveolar concentration [74]. These

610   outcomes are consistent with established deposition mechanisms, such as inertial impaction

611   and gravitational sedimentation, which are influenced by particle size and aerodynamic

612   diameter. Notably, particles in the 0.1 µm - 1.5 µm range exhibit minimal sensitivity to flow

613   rate (500 mL/s – 2000 mL/s) but significant responsiveness to breath-holding duration [75].

614   This can be challenging considering the different inspiratory capacities of patients suffering

615   from respiratory diseases. Micron-sized particles, such as mesoporous silica particles

616   (MSPs), offer controlled drug release, enhanced efficiency, and stability [76, 77]. Deposition

617   profiles are intricately linked to individual lung characteristics and breathing patterns [78,

618   79]. The balance between mucociliary advection and diffusion in the mucus layer affects

619   drug availability across lung regions, with breath control techniques enhancing deep lung

620   delivery for 0.5 µm - 2 µm aerosols [80]. Precise particle engineering is essential to maximize

621   therapeutic efficacy, minimize side effects, and ensure reliable drug delivery making the 3D-

622   printed micromixers coupled with spray drying a useful tool for tuning particle size. In this

623   work, we have demonstrated that controlling particle precipitation using microfluidic

624   micromixers coupled with spray drying can provide us with a feasible tool for this purpose.

625   Haemolysis testing serves as a critical *in vitro* method for evaluating both the membrane-

626   damaging potential and biocompatibility of inhaled particles in biological systems,

627   particularly in the alveolar region where systemic exposure to red blood cells occurs. Our

628   study demonstrated that AZM-loaded heparin microparticles exhibited lower haemolytic

629   toxicity compared to the unencapsulated drug [81, 82]. The minimal haemolytic activity

630   observed under tested conditions supports the safety profile of the developed spray-dried

631   formulation, validating its suitability for pharmaceutical applications and safety for

632   pulmonary administration.

633   In pulmonary drug delivery, the relationship between epithelial lining fluid (ELF) volume

634   and drug concentration is crucial for ensuring therapeutic efficacy. ELF constitutes

635   approximately 0.39 % of total lung capacity, with volumes ranging from 23.4 mL in healthy

636   adults to 15.6 mL in individuals with compromised pulmonary function [83-85]. In our study,

637   we targeted concentrations of 20 µg/mL of AZM in ELF, exceeding by 5-fold the reported

638   epidemiological cut-offs (ECOFFs) in *H. influenzae* for AZM (4 mg/L [86]) while

639   maintaining higher lung cell viability (> 94 %), without toxicity on macrophage cells.

640   Bearing in mind a drug loading of 3.3 % and an FPF of 57.2 %, the inhalation of 25 mg of

641   dry powder would result in 472 µg of AZM delivered to the lung. Assuming 23.4 mL of ELF,

642   the AZM concentration in the lung would be 20 µg/mL which is well above the ECOFF. The

643   final regime of administration should be adjusted based on the pharmacokinetic profile of

644   AZM in the lung.

Conclusion

646   This work introduces an innovative approach to pulmonary drug delivery by combining 3D-

647   printed microfluidic devices with spray-drying technology to produce AZM microparticles

648   for efficient pulmonary delivery. This study demonstrates the integration of advanced

649   technologies to enhance pulmonary drug deposition, showing promise for improved

650   therapeutic outcomes. This combined approach allows for precise control over particle size,

651   distribution, and encapsulation efficiency while promoting enhanced mixing and yield. The

652   scalability, reproducibility, and rapid process development capabilities of this integrated

653   approach facilitate the optimization of formulation parameters and the production of stable,

654   customizable particles with improved aerodynamic properties for lung delivery.

Acknowledgments

References

662 1. Gondhale-Karpe, P., *Novel Techniques in Pulmonary Drug Delivery Systems*, in
663   *Novel Technologies in Biosystems, Biomedical & Drug Delivery*. 2023, Springer. p.
664   221-239.
665 2. Ibrahim, M., R. Verma, and L. Garcia-Contreras, *Inhalation drug delivery devices:*
666   *technology update.* Medical Devices: Evidence and Research, 2015: p. 131-139.
667 3. Kumar, R., et al., *Nanotechnology-assisted metered-dose inhalers (MDIs) for high-*
668   *performance pulmonary drug delivery applications.* Pharmaceutical research, 2022.
669   **39**(11): p. 2831-2855.
670 4. de Pablo, E., et al., *Nebulised antibiotherapy: conventional versus nanotechnology-*
671   *based approaches, is targeting at a nano scale a difficult subject?* Annals of
672   translational medicine, 2017. **5**(22).
673 5. Celi, S.S., et al., *Co-Delivery of a High Dose of Amphotericin B and Itraconazole by*
674   *Means of a Dry Powder Inhaler Formulation for the Treatment of Severe Fungal*
675   *Pulmonary Infections.* Pharmaceutics, 2023. **15**(11): p. 2601.
676 6. Kuga, K., et al., *Effect of transient breathing cycle on the deposition of micro and*
677   *nanoparticles on respiratory walls.* Computer Methods and Programs in
678   Biomedicine, 2023. **236**: p. 107501.
679 7. Knap, K., et al., *Inhalable microparticles as drug delivery systems to the lungs in a*
680   *dry powder formulations.* Regenerative Biomaterials, 2023. **10**: p. rbac099.
681 8. Chandel, A., et al., *Recent advances in aerosolised drug delivery.* Biomedicine &
682   Pharmacotherapy, 2019. **112**: p. 108601.
683 9. Ossebaard, H.C., et al., *Turning green: the impact of changing to more eco-friendly*
684   *respiratory healthcare. A carbon and cost analysis of Dutch prescription data.*
685   medRxiv, 2021: p. 2021.11. 20.21266571.
686 10. Liu, H., et al., *Computational investigation of flow characteristics and particle*
687   *deposition patterns in a realistic human airway model under different breathing*
688   *conditions.* Respiratory Physiology & Neurobiology, 2023. **314**: p. 104085.
689 11. Rahman, M., et al., *Numerical study of nano and micro pollutant particle transport*
690   *and deposition in realistic human lung airways.* Powder Technology, 2022. **402**: p.
691   117364.
692 12. de Pablo, E., et al., *Targeting lung macrophages for fungal and parasitic pulmonary*
693   *infections with innovative amphotericin B dry powder inhalers.* International journal
694   of pharmaceutics, 2023. **635**: p. 122788.
695 13. Orea-Tejeda, A., et al., *Dynapenia and Sarcopenia in Post-COVID-19 Syndrome*
696   *Hospitalized Patients Are Associated with Severe Reduction in Pulmonary Function.*
697   Journal of Clinical Medicine, 2023. **12**(20): p. 6466.
698 14. Ribeiro Baptista, B., et al., *Identification of factors impairing exercise capacity after*
699   *severe COVID-19 pulmonary infection: a 3-month follow-up of prospective*
700   *COVulnerability cohort.* Respiratory Research, 2022. **23**(1): p. 68.
701 15. Kjellberg, S., et al., *Impaired function in the lung periphery following COVID-19 is*
702   *associated with lingering breathing difficulties.* Physiological Reports, 2024. **12**(2):
703   p. e15918.
704 16. Tyagi, N., et al., *3D printing technology in the pharmaceutical and biomedical*
705   *applications: a critical review.* Biomedical Materials & Devices, 2024. **2**(1): p. 178-
706   190.

707   17.   Haque, S., et al., *The applications of 3D printing in pulmonary drug delivery and*
708   *treatment of respiratory disorders.* Current Pharmaceutical Design, 2018. **24**(42): p.
709   5072-5080.
710   18.   Serrano, D., et al., *3D Printing Technologies in Personalized Medicine,*
711   *Nanomedicines, and Biopharmaceuticals. Pharmaceutics 15*. 2023.
712   19.   Anaya, B.J., et al., *Engineering of 3D printed personalized polypills for the*
713   *treatment of the metabolic syndrome.* International Journal of Pharmaceutics, 2023.
714   **642**: p. 123194.
715   20.   Kara, A., et al., *3D Printing Technologies for Personalized Drug Delivery*, in
716   *Emerging Drug Delivery and Biomedical Engineering Technologies*. 2023, CRC
717   Press. p. 31-47.
718   21.   Yuste, I., et al., *Engineering 3D-printed advanced healthcare materials for*
719   *periprosthetic joint infections.* Antibiotics, 2023. **12**(8): p. 1229.
720   22.   Wu, K., et al., *Recent progress of microfluidic chips in immunoassay.* Frontiers in
721   Bioengineering and Biotechnology, 2022. **10**: p. 1112327.
722   23.   Osouli-Bostanabad, K., et al., *Microfluidic manufacture of lipid-based*
723   *nanomedicines.* Pharmaceutics, 2022. **14**(9): p. 1940.
724   24.   Pugia, M.J., et al., *Microfluidic tool box as technology platform for hand-held*
725   *diagnostics.* Clinical chemistry, 2005. **51**(10): p. 1923-1932.
726   25.   Kara, A., et al., *Engineering 3D printed microfluidic chips for the fabrication of*
727   *nanomedicines.* Pharmaceutics, 2021. **13**(12): p. 2134.
728   26.   Patil, A., et al., *Combined microfluidics and drying processes for the continuous*
729   *production of micro-/nanoparticles for drug delivery: a review.* Drying Technology,
730   2023. **41**(10): p. 1533-1568.
731   27.   Segal, L.N., et al., *Randomised, double-blind, placebo-controlled trial with*
732   *azithromycin selects for anti-inflammatory microbial metabolites in the*
733   *emphysematous lung.* Thorax, 2017. **72**(1): p. 13-22.
734   28.   Oliver, M.E. and T.S. Hinks, *Azithromycin in viral infections.* Reviews in medical
735   virology, 2021. **31**(2): p. e2163.
736   29.   Leal, T., et al., *Azithromycin attenuates Pseudomonas-induced lung inflammation by*
737   *targeting bacterial proteins secreted in the cultured medium.* Frontiers in
738   immunology, 2016. **7**: p. 499.
739   30.   Gualdoni, G.A., et al., *Azithromycin inhibits IL-1 secretion and non-canonical*
740   *inflammasome activation.* Scientific reports, 2015. **5**(1): p. 12016.
741   31.   Saris, A., et al., *The Azithromycin Pro-Drug CSY5669 Boosts Bacterial Killing*
742   *While Attenuating Lung Inflammation Associated with Pneumonia Caused by*
743   *Methicillin-Resistant Staphylococcus aureus.* Antimicrobial Agents and
744   Chemotherapy, 2022. **66**(9): p. e02298-21.
745   32.   Joelsson, J.P., et al., *Azithromycin ameliorates sulfur dioxide-induced airway*
746   *epithelial damage and inflammatory responses.* Respiratory research, 2020. **21**: p.
747   1-11.
748   33.   Patel, A., et al., *Azithromycin in combination with ceftriaxone reduces systemic*
749   *inflammation and provides survival benefit in a murine model of polymicrobial*
750   *sepsis.* Antimicrobial agents and chemotherapy, 2018. **62**(9): p. 10.1128/aac. 00752-
751   18.

752 34. Mangiafico, M., A. Caff, and L. Costanzo, *The role of heparin in COVID-19: an*
753   *update after two years of pandemics.* Journal of Clinical Medicine, 2022. **11**(11): p.
754   3099.
755 35. Costanzo, L., et al., *Coagulopathy, thromboembolic complications, and the use of*
756   *heparin in COVID-19 pneumonia.* Journal of Vascular Surgery: Venous and
757   Lymphatic Disorders, 2020. **8**(5): p. 711-716.
758 36. Tree, J.A., et al., *Unfractionated heparin inhibits live wild type SARS-CoV-2 cell*
759   *infectivity at therapeutically relevant concentrations.* British Journal of
760   Pharmacology, 2021. **178**(3): p. 626-635.
761 37. Zang, L., et al., *Not Just Anticoagulation—New and Old Applications of Heparin.*
762   Molecules, 2022. **27**(20): p. 6968.
763 38. Anaya, B.J., et al., *Heparin-azithromycin microparticles show anti-inflammatory*
764   *effects and inhibit SARS-CoV-2 and bacterial pathogens associated to lung*
765   *infections.* Carbohydrate Polymers, 2024: p. 122930.
766 39. Ongoren, B., et al., *Leveraging 3D-printed microfluidic micromixers for the*
767   *continuous manufacture of melatonin loaded SNEDDS with enhanced antioxidant*
768   *activity and skin permeability.* International Journal of Pharmaceutics, 2024: p.
769   124536.
770 40. Kara, A., et al., *Continuous manufacturing of cocrystals using 3d-printed*
771   *microfluidic chips coupled with spray coating.* Pharmaceuticals, 2023. **16**(8): p.
772   1064.
773 41. Lechanteur, A. and B. Evrard, *Influence of composition and spray-drying process*
774   *parameters on carrier-free DPI properties and behaviors in the lung: A review.*
775   Pharmaceutics, 2020. **12**(1): p. 55.
776 42. Gholizadeh-Hashjin, A., et al., *Compatibility study of formoterol fumarate-lactose*
777   *dry powder inhalation formulations: Spray drying, physical mixture and*
778   *commercial DPIs.* Journal of Drug Delivery Science and Technology, 2024. **95**: p.
779   105538.
780 43. Malamatari, M., et al., *Spray drying for the preparation of nanoparticle-based drug*
781   *formulations as dry powders for inhalation.* Processes, 2020. **8**(7): p. 788.
782 44. Al-Zoubi, N., et al., *Spray drying for direct compression of pharmaceuticals.*
783   Processes, 2021. **9**(2): p. 267.
784 45. Baumann, J.M., M.S. Adam, and J.D. Wood, *Engineering advances in spray drying*
785   *for pharmaceuticals.* Annual review of chemical and biomolecular engineering,
786   2021. **12**(1): p. 217-240.
787 46. Ongoren, B., et al., *Leveraging 3D-printed microfluidic micromixers for the*
788   *continuous manufacture of melatonin loaded SNEDDS with enhanced antioxidant*
789   *activity and skin permeability.* International Journal of Pharmaceutics, 2024. **663**: p.
790   124536.
791 47. ICH, E., *Impurities: Guidelines for residual solvents Q3C (R5)*. 2011, ICH Geneva,
792   Switzerland.
793 48. Welton, T., *Solvents and sustainable chemistry.* Proceedings of the Royal Society A:
794   Mathematical, Physical and Engineering Sciences, 2015. **471**(2183): p. 20150502.
795 49. Al-Hakkani, M.F., *A rapid, developed and validated RP-HPLC method for*
796   *determination of azithromycin.* SN Applied Sciences, 2019. **1**(3): p. 222.

797 50.   Javaid, M.U., T.A. Cheema, and C.W. Park, *Analysis of passive mixing in a
798   serpentine microchannel with sinusoidal side walls.* Micromachines, 2017. **9**(1): p.
799   8.
800 51.   Chen, X. and J. Shen, *Simulation and experimental analysis of a SAR micromixer
801   with F-shape mixing units.* Analytical Methods, 2017. **9**(12): p. 1885-1890.
802 52.   Ta, B.Q., et al., *Geometric effects on mixing performance in a novel passive
803   micromixer with trapezoidal-zigzag channels.* Journal of Micromechanics and
804   Microengineering, 2015. **25**(9): p. 094004.
805 53.   Technology, N.I.o.S.a. *Thermophysical Properties of Fluid Systems.* [cited 2023
806   11]; Available from: https://webbook.nist.gov/chemistry/fluid/.
807 54.   Javaid, M.U., T.A. Cheema, and C.W. Park, *Analysis of Passive Mixing in a
808   Serpentine Microchannel with Sinusoidal Side Walls.* Micromachines, 2018. **9**(1): p.
809   8.
810 55.   Anaya, B.J., et al., *Heparin-azithromycin microparticles show anti-inflammatory
811   effects and inhibit SARS-CoV-2 and bacterial pathogens associated to lung
812   infections.* Carbohydrate Polymers, 2025. **348**: p. 122930.
813 56.   Serrano, D.R., et al., *Oral particle uptake and organ targeting drives the activity of
814   amphotericin B nanoparticles.* Molecular pharmaceutics, 2015. **12**(2): p. 420-431.
815 57.   Smith, L., et al., *Orally bioavailable and effective buparvaquone lipid-based
816   nanomedicines for visceral leishmaniasis.* Molecular pharmaceutics, 2018. **15**(7): p.
817   2570-2583.
818 58.   Santamaría, K.J., et al., *Engineering 3D printed gummies loaded with metformin for
819   paediatric use.* Gels, 2024. **10**(10): p. 620.
820 59.   Pineros, I., et al., *Analgesic and anti-inflammatory controlled-released injectable
821   microemulsion: Pseudo-ternary phase diagrams, in vitro, ex vivo and in vivo
822   evaluation.* European journal of pharmaceutical sciences, 2017. **101**: p. 220-227.
823 60.   Jones, R.N., et al., *Validation of NCCLS macrolide (azithromycin, clarithromycin,
824   and erythromycin) interpretive criteria for Haemophilus influenzae tested with the
825   Haemophilus test medium.* Diagnostic microbiology and infectious disease, 1994.
826   **18**(4): p. 243-249.
827 61.   Marple, V.A., et al., *Next generation pharmaceutical impactor (a new impactor for
828   pharmaceutical inhaler testing). Part I: Design.* Journal of aerosol medicine, 2003.
829   **16**(3): p. 283-299.
830 62.   Udvardi, B., et al., *Effects of particle size on the attenuated total reflection spectrum
831   of minerals.* Applied spectroscopy, 2017. **71**(6): p. 1157-1168.
832 63.   Tran, T.H., et al., *Microfluidic approach for highly efficient synthesis of heparin-
833   based bioconjugates for drug delivery.* Lab on a Chip, 2012. **12**(3): p. 589-594.
834 64.   Abo-Zeid, Y., et al., *Antimicrobial activity of azithromycin encapsulated into PLGA
835   NPs: a potential strategy to overcome efflux resistance.* Antibiotics, 2022. **11**(11): p.
836   1623.
837 65.   Li, X., et al., *Encapsulation of azithromycin into polymeric microspheres by reduced
838   pressure-solvent evaporation method.* International journal of pharmaceutics, 2012.
839   **433**(1-2): p. 79-88.
840 66.   Anaya, B.J., et al., *Heparin-azithromycin microparticles show anti-inflammatory
841   effects and inhibit SARS-CoV-2 and bacterial pathogens associated to lung
842   infections.* Carbohydr Polym, 2025. **348**(Pt B): p. 122930.

843 67. *SPIRIVA® HANDIHALER® (tiotropium bromide inhalation powder) for oral
844   inhalation use. Available at: https://content.boehringer-
845   ingelheim.com/DAM/7e63d875-6ffb-407d-a561-
846   af1e012045e5/spiriva%20handihaler-us-pi.pdf. Accessed date: 01/02/2025.*
847 68. Clark, A.R., J.G. Weers, and R. Dhand, *The confusing world of dry powder
848   inhalers: it is all about inspiratory pressures, not inspiratory flow rates.* Journal of
849   aerosol medicine and pulmonary drug delivery, 2020. **33**(1): p. 1-11.
850 69. Vartiainen, V.A., et al., *High inhaler resistance does not limit successful inspiratory
851   maneuver among patients with asthma or COPD.* Expert Opinion on Drug Delivery,
852   2023. **20**(3): p. 385-393.
853 70. Gauani, H., et al., *Effect of inhalation profile on delivery of treprostinil palmitil
854   inhalation powder.* Pharmaceutics, 2023. **15**(3): p. 934.
855 71. Chavan, V. and R. Dalby, *Novel system to investigate the effects of inhaled volume
856   and rates of rise in simulated inspiratory air flow on fine particle output from a dry
857   powder inhaler.* Aaps Pharmsci, 2002. **4**: p. 7-12.
858 72. Wang, B., et al., *Effect of airflow rate on droplet deposition of an impinging-jet
859   inhaler in the human respiratory tract.* International Journal of Pharmaceutics,
860   2024. **661**: p. 124408.
861 73. Kartanas, T., et al., *Mechanism of droplet-formation in a supersonic microfluidic
862   spray device.* Applied Physics Letters, 2020. **116**(15).
863 74. Dudhat, K.R. and H.V. Patel, *Influence of Particle Size and Particle Deposition of
864   Inhaled Medication in Lung Disease: A Comrehensive Review.* International Journal
865   of Pharmaceutical Sciences and Drug Research, 2022: p. 141-157.
866 75. Min, H.J., E.P. Stride, and S.J. Payne, *In silico investigation of the effect of particle
867   diameter on deposition uniformity in pulmonary drug delivery.* Aerosol Science and
868   Technology, 2023. **57**(4): p. 318-328.
869 76. Pacheco, J.E.C., et al., *Inhalable porous particles as dual micro-nano carriers
870   demonstrating efficient lung drug delivery for treatment of tuberculosis.* Journal of
871   Controlled Release, 2024. **369**: p. 231-250.
872 77. van der Zwaan, I., et al., *Influence of particle diameter on aerosolization
873   performance and release of budesonide loaded mesoporous silica particles.*
874   European Journal of Pharmaceutical Sciences, 2024: p. 106828.
875 78. Rissler, J., et al., *An experimental study on lung deposition of inhaled 2 μm particles
876   in relation to lung characteristics and deposition models.* Particle and Fibre
877   Toxicology, 2023. **20**(1): p. 40.
878 79. Barrio-Perotti, R., et al., *Predicting particle deposition using a simplified 8-path in
879   silico human lung prototype.* Journal of Breath Research, 2023. **17**(4): p. 046002.
880 80. Chakravarty, A., et al., *Pulmonary drug delivery and retention: A computational
881   study to identify plausible parameters based on a coupled airway-mucus flow
882   model.* PLoS computational biology, 2022. **18**(6): p. e1010143.
883 81. Shi, J., et al., *Hemolytic properties of synthetic nano-and porous silica particles: the
884   effect of surface properties and the protection by the plasma corona.* Acta
885   Biomaterialia, 2012. **8**(9): p. 3478-3490.
886 82. Thakare, P., et al., *Exploring the potential of three-layered self-assembled
887   biomaterial-based dry powder inhaler for enhanced structural integrity and lung
888   deposition of bioactive Lysozyme.* BioNanoScience, 2024. **14**(3): p. 3341-3354.

889 83. Rodvold, K.A., J.M. George, and L. Yoo, *Penetration of anti-infective agents into*
890 *pulmonary epithelial lining fluid: focus on antibacterial agents.* Clinical
891 pharmacokinetics, 2011. **50**: p. 637-664.
892 84. Drwiega, E.N. and K.A. Rodvold, *Penetration of antibacterial agents into*
893 *pulmonary epithelial lining fluid: an update.* Clinical pharmacokinetics, 2022.
894 **61**(1): p. 17-46.
895 85. Chinard, F.P., *Quantitative assessment of epithelial lining fluid in the lung.*
896 American Journal of Physiology-Lung Cellular and Molecular Physiology, 1992.
897 **263**(6): p. L617-L618.
898 86. *EUCAST Clinical breakpoints - breakpoints and guidance. Available at:*
899 *https://www.eucast.org/clinical_breakpoints. Date: 01/02/2025.*

900